Solubility Effects on Growth and Dissolution of Methane Hydrate Needles

Sivakumar Subramanian[(1)]*, E. Dendy Sloan, Jr.[(2)]

[(1)] ChevronTexaco Exploration and Production Technology Company, Houston, Texas 77082, USA;
[(2)] Center for Hydrate Research, Colorado School of Mines, Golden, CO 80401 USA

Growth of hydrate needles was observed upon cooling of a quiescent methane-water system. The needles grew from the vapor-liquid interface into the bulk aqueous phase after a hydrate film had first formed at the vapor-liquid interface. Stepwise heating of the system across the three phase liquid water-hydrate-vapor equilibrium boundary caused a stepwise dissolution of needles even when the pressure-temperature conditions in relation to the Lw-H-V curve were favorable for methane hydrate existence. Visual observations coupled with Raman spectra were used to identify the growth and dissolution mechanism of needles. It is concluded that hydrate needle growth is sustained by methane dissolved in the bulk aqueous phase and not the vapor phase. This is attributed to the solubility of methane in water being lower in the presence of a hydrate phase when compared to solubility in the absence of a hydrate phase. The solubility trends combined with metastability upon hydrate formation and heat transfer effects upon crystallization cause the needle morphology to predominate in this system.

1 Introduction

Some of the most challenging and intriguing questions regarding hydrates concern kinetics of formation and growth. The majority of the experimental effort to understand hydrate kinetics pertains to collecting macroscopic data such as pressure, temperature, turbidity point, particle size, and gas consumption. Attempts have also been made to obtain microscopic and mesoscopic experimental data from light scattering, single crystal growth, and spectroscopy to obtain mechanistic insights into kinetics of hydrate formation and growth. Well known models in the literature treat global kinetics of hydrate formation and growth as being a net result of mass transfer, heat transfer, and intrinsic reaction kinetics associated with the process. However, simplifying assumptions usually need to be made to reduce the complexity of the modeling approach (Englezos et al., 1987; Skovborg and Rasmussen, 1994; Freer, 2000). The driving force for mass transfer in this process is concentration gradient of species between the hydrate phase and the associated fluid phases.

The concentration of methane in water is of the order of 10^{-3} mole fraction at 303 K and 10 MPa compared to a methane mole fraction of ~ 0.15 in the hydrate phase. It has been suggested that this two orders of magnitude difference in methane concentration causes hydrate formation and growth to preferentially occur at the gas-water interface where methane will be more readily available for incorporation into the growing hydrate phase (Sloan, 1998). To accurately model the global kinetics of this process, the concentrations of methane in the different phases need to be known.

As a result, solubility of methane in the water phase is a crucial parameter for modeling methane hydrate formation & growth kinetics. In this work, results from visual and Raman experiments were used to decipher the mechanism of hydrate growth in a quiescent methane-water system. The effect of methane solubility on hydrate growth and dissolution was explored.

2 Experimental Methods

The basic high pressure experimental apparatus used for the present study has been described elsewhere in detail (Subramanian and Sloan, 1999). It was slightly modified to enable video capturing of cell contents in addition to collection of Raman spectra.

For both visual and Raman experiments, the 34 MPa high pressure optical cell was first loaded with 0.8 mL of deionized water and pressurized to 31.7 MPa with research grade methane gas using a gas booster. The temperature was stabilized at 24 ^{o}C by circulating coolant through the cell body. Cell contents were thoroughly shaken to ensure equilibration and facilitate the concentration of methane in the water phase to reach the equilibrium solubility value at the set pressure-temperature condition. The cell was mounted on a precision XY spectroscopic translation stage. A CCD camera in conjunction with a TV-VCR system was used to capture images during the course of the visual experiment. Cell temperature and pressure were monitored throughout the experiments.

The first part of the visual experiment involved forming hydrates in the cell by continuous cooling under non-stirred conditions. The cooling rate was 0.6 ^{o}C per minute and final temperature of cell contents was 5.2 ^{o}C. Temperature was maintained at 5.2 ^{o}C for twenty minutes. The next part of the visual experiment involved stepwise heating under non-stirred conditions from 5.2 ^{o}C to 23.4 ^{o}C, which is about 0.2 ^{o}C higher than the predicted hydrate dissociation temperature of 23.2 ^{o}C for methane at 31.6 MPa. The intermediate temperatures in the stepwise heating process were 10.5, 15.3, 20.3, 21.5, and 22.6 ^{o}C. The Raman experiment was similar to the first part of the visual experiment except that Raman spectra of the aqueous phase were collected at different stages of the continuous cooling process.

Figure 1 depicts the cell pressure-temperature profile during the experiment. The cell pressure (MPa) almost follows the same trend as the cell temperature (^{o}C) with time.

* Corresponding author. E-mail: sisu@chevrontexaco.com

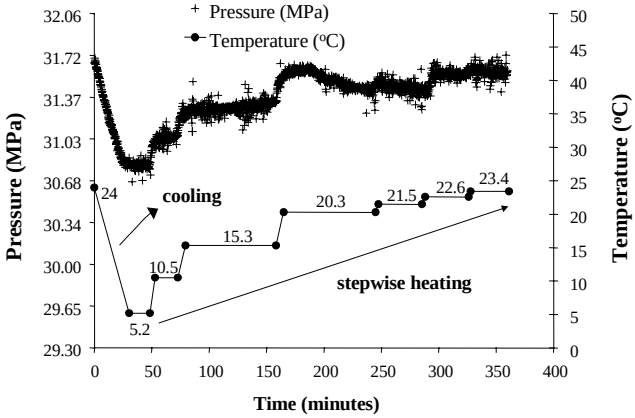

Fig. 1 Cell pressure-temperature profile during continuous cooling and stepwise heating

3 Results and Discussion

3.1 Hydrate Growth During Continuous Cooling. Fig. 2 shows a sequence of images of the cell contents at different stages of the cooling process. Starting from 24 ^{o}C, it can be seen that methane hydrate did not form in the system until 15.2 ^{o}C. This corresponded to about 8 ^{o}C supercooling. At this temperature, hydrates appeared to nucleate somewhere along the vapor-liquid interface and grow as a film that spread across the entire interface within tens of seconds. Hydrates also appeared to grow on the optical window above the vapor-liquid interface. This is attributed to the conversion of a thin film of water on the window to hydrates; the thin film arising from shaking of the cell contents prior to cooling.

After this nucleation event, the entire vapor-liquid interface and the vapor phase looked 'hydrated'. Upon cooling below 15.2 ^{o}C, it can be seen from Fig. 2 that hydrate needles started to appear at the vapor-liquid interface at 8.9 ^{o}C. Further cooling to 7.3 caused the needles to grow in length and extend from the bottom of the hydrated vapor-liquid interface down into the bulk aqueous phase. At 5.2 ^{o}C, the needles occupied a significant portion of the bulk aqueous phase.

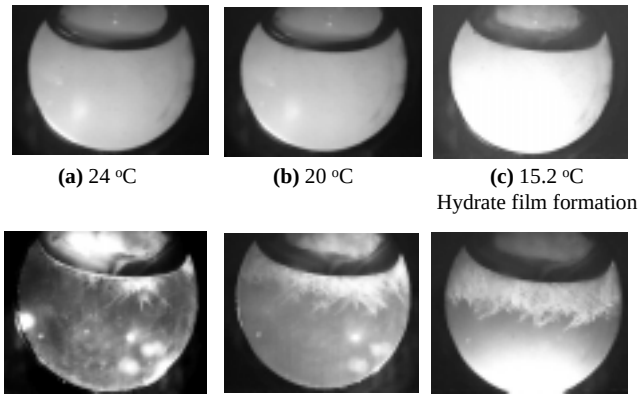

Fig. 2 A sequence of images of the cell contents at different stages of the continuous cooling process.

From pressure-temperature data (Fig. 1), cell pressure was 30.82 MPa at the end of cooling indicating a 0.9 MPa gradual drop in cell pressure during the cooling process. The pressure trace lacked any discontinuities or changes in slope as would be expected upon hydrate formation in a closed vapor-liquid water system due to incorporation of large volumes of gas into the hydrate (Sloan, 1998).

In order to decipher the growth mechanism of hydrate needles shown in Fig. 2, the source of methane molecules contributing to sustained growth of hydrate needles needs to be identified. There are two probable sources of methane molecules - the methane gas phase and the bulk aqueous phase. For the case of gas phase as source, diffusion of methane to the aqueous phase and the growing hydrate surface would have to occur through open microscopic cracks/pores in the 'hydrated' vapor-liquid interface. For the case of bulk aqueous phase as source, a concentration gradient is necessary to drive diffusion of methane through the aqueous phase towards the needles extending from the vapor-liquid interface.

A discontinuity in the pressure trace in Fig. 1 would have been a clear evidence for the gas phase acting as source. The absence of a sudden pressure drop in spite of hydrate formation and needle growth in the system suggests that the gas phase may not have experienced the demand for methane molecules to sustain needle growth. Hydrate film formation at the vapor-liquid interface may have been a barrier to mass transfer effectively 'sealing off' and isolating the bulk aqueous phase from the gas phase. This implies that the bulk aqueous phase, not the gas phase, may have been the source of methane molecules needed to sustain needle growth upon further cooling.

For this mechanism to operate, there should have been a driving force for methane molecules to diffuse towards the vapor-liquid interface from the bulk aqueous phase, with a decrease in temperature. The existence of such a driving force can be understood from equilibrium solubilities of methane in water in the absence and presence of methane hydrates as illustrated in Fig. 3. This general plot has been generated for a given pressure and so can be thought of as a T-x diagram. The solid line represents the concentration of methane dissolved in

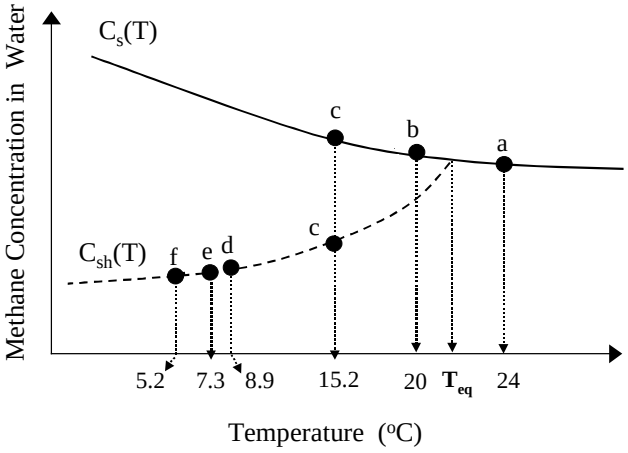

Fig. 3 A schematic illustration of temperature dependencies of equilibrium methane concentration in liquid water. The scale of the vertical axis is arbitrary. Points **a** through **f** correspond to different temperatures during the continuous cooling process.

water, C_s, when only methane gas and liquid water are in equilibrium with each other. The temperature dependency of this curve has been well established (Culberson and McKetta, 1951). The dashed line represents the concentration of methane dissolved in water, C_{sh}, when methane hydrate and liquid water are in equilibrium with each other. The temperature dependency of this curve is proposed based on observations and calculations for other hydrate forming systems (Kimuro et al., 1994; Yamane and Aya, 1995; Makogon, 1996; Zatsepina and Buffett, 1997; Ohmura et al., 1999). The two curves in Fig. 3, C_s (T) and C_{sh} (T), intersect at the equilibrium dissociation temperature, T_{eq}, for the given system pressure.

As can be seen from Fig. 3, at temperatures lower than T_{eq}, the two curves have opposite characteristics. The curve for C_s(T) suggests that methane's solubility increases with decreasing temperature. The curve for C_{sh}(T) suggests that methane's solubility decreases with decreasing temperature. These two very different equilibrium solubility curves for methane in water when combined together can explain the driving force, with decreasing temperature, for methane dissolved in water to diffuse towards the vapor-liquid interface and sustain the growth of hydrate needles.

3.2 Aqueous Phase as a Source of Methane. Let's consider the series of snapshots presented in Fig.2. Each snapshot in the sequence corresponds to a different temperature. These temperatures and the probable concentration of methane in liquid water at these temperatures are marked in Fig. 3. The marks are either on the curve for C_s (T) or the curve for C_{sh} (T) depending on the absence or presence of hydrates in the cell at a given temperature.

From Figs. 2a and 2b, it can be seen that hydrates were not present at 24 and 20 ^oC and so corresponding circular marks are placed on the C_s (T) curve in Fig. 3. The hydrate film first formed at 15.2 ^oC (Fig. 2c). Therefore, circular marks are placed on both the curves, C_s (T) and C_{sh} (T) for this case. From Fig. 2d, 2e, and 2f, hydrates were present in the system at temperatures of 8.9, 7.3, and 5.2 ^oC. Therefore, circular marks corresponding to these temperatures are placed on the C_{sh} (T) curve in Fig. 3.

By tracking the circular marks in Fig. 3, it can be seen that cooling from 24 ^oC caused the concentration of methane dissolved in water to increase along the C_s(T) curve (points a and b). This increase in methane concentration in the bulk aqueous phase is expected till the temperature of 15.2 ^oC when hydrates first nucleated in the system at the vapor-liquid interface. The hydrate then rapidly grew as a film at this temperature across the vapor-liquid interface and engulfed the entire interface.

At this point, from Fig., 3, the actual concentration of methane in the bulk aqueous phase was at point c on the C_s(T) curve. However, since hydrates were present in the system, the equilibrium concentration of methane in the bulk aqueous phase must have corresponded to point c on the C_{sh} (T) curve. Therefore, the growth of the hydrate film at the interface resulted in the bulk aqueous phase being supersaturated in methane.

Upon further cooling, the equilibrium solubility of methane in water had to follow the C_{sh} (T) curve. This is because the liquid water phase was in contact with a methane hydrate film. Following this curve, the equilibrium concentrations of methane in the bulk aqueous phase decreased with decreasing temperature. At point d on the C_{sh} (T) curve (8.9 ^oC), the bulk aqueous phase was considerably supersaturated in methane.

Although the bulk aqueous phase was supersaturated in methane, the water that was in immediate contact with the methane hydrate film at the vapor-liquid interface must have had the equilibrium methane concentration of C_{sh} (T=8.9), i.e. the concentration corresponding to point d in Fig. 3. It is hypothesized that this difference in concentrations of methane between the bulk aqueous phase and interfacial water in contact with the hydrate film caused mass transfer of methane from the bulk aqueous phase to the bottom of the hydrate film. The driving force can be stated as the concentration difference C_s (T=15.2) – C_{sh} (T=8.9). This supply of methane towards the interface favored the growth of hydrates at the bottom of the hydrate film. Due to the heat of formation associated with hydrate growth, the local temperature at the bottom of the hydrate film may have been higher than the rest of the cell. Since the system was quiescent and the cooling rate of the bulk aqueous phase (0.6 ^oC per minute) was high, further crystal growth may have been heat transfer limited. It is well established that needle morphologies are common in heat transfer limited crystal growth (Chalmers, 1964), which due to their high surface area to volume ratio have better heat dissipation capability. Thus, we hypothesize that the needle morphology became established very quickly at the bottom of the hydrate film in order to sustain crystal growth. The evidence for this can be seen in Fig. 2d.

Once hydrate needles started forming at the underside of the interfacial hydrate film, it is hypothesized that they caused steep concentration gradients of methane around their surfaces, steeper than those over the almost planar nature of the underside of the hydrate film at the vapor-liquid interface. These steep concentration gradients resulted in higher methane mass fluxes from the bulk aqueous phase to the needles thus causing preferential growth of needles into the bulk aqueous phase.

Upon further cooling, it is hypothesized that the equilibrium solubility of methane in the aqueous phase tracked the C_{sh} (T) curve and dropped from point d to e to f. The decreasing solubility caused increasing methane mass flux from the bulk aqueous phase to the hydrate needles extending from the vapor-liquid interface. This should have resulted in extensive growth of needles over this temperature range. The evidence for this can be observed in Figs. 2d, 2e, and 2f.

As hydrate needles grew, the bulk aqueous phase relieved its supersaturation and methane concentration in the bulk aqueous progressively approached the equilibrium solubility value. After continuous cooling, the cell was held at the final temperature of 5.2 ^oC for a period of 20 minutes. It is hypothesized that during this time, the concentration of methane in the bulk aqueous phase reached the equilibrium solubility (point f in Fig. 3), and further supply of methane to the needles was stopped, thereby stopping any further needle growth. This is in agreement with the experimental observations in Fig. 2f. Needles stopped growing when the system was allowed to stabilize at the final temperature of 5.2 ^oC for 20 minutes.

3.3 Raman Evidence for Proposed Mechanism.

Further evidence for bulk aqueous phase acting as the source of methane molecules for sustained needle growth can be obtained from Raman spectra collected during the continuous cooling process. Several researchers have

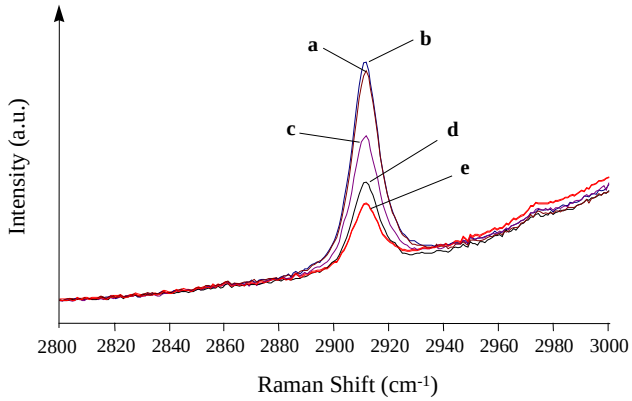

Fig. 4 A series of Raman spectra of dissolved methane collected at different temperatures during the continuous cooling process. Spectra marked **a** through **e** correspond to temperatures of 24, 20, 15.6, 10.2, and, 2.8 ^{o}C, respectively.

used Raman spectroscopy to study hydrates and mechanisms involved in hydrate formation (Sum et al., 1997; Tulk et al., 2000; Uchida et al., 2000, Subramanian et al., 2000). From the theory of Raman spectroscopy, it can be shown that band areas in the Raman spectrum of a molecule in a particular environment are directly proportional to the concentration of the molecule in that environment (Szymanski, 1967; Long, 1977). The band areas also depend on other quantities such as radiant intensity of the incident excitation source, the excitation frequency, the Raman shift corresponding to the vibrational mode responsible for the band, temperature, and the derived polarizability tensor. This complicated relationship between band areas in a Raman spectrum and the factors affecting them have raised questions about the usefulness of Raman spectroscopy in obtaining definitive quantitative compositional information about the solid hydrate phase (Tulk et al., 2000).

Nonetheless, Raman spectra of the aqueous phase can be used to draw qualitative conclusions about changes in the concentration of methane in the bulk aqueous phase during the continuous cooling process. Specifically, area under the band centered at about 2911 cm^{-1} corresponding to the symmetric C-H stretching vibrational mode of methane dissolved in water (Subramanian et al., 1999) can be used to qualitatively track the concentration of methane in the bulk aqueous phase. By monitoring the intensity (and hence area under this band) during the continuous cooling process, it is possible to verify the proposed mechanism of the bulk aqueous phase acting as a source of methane for needle growth. Due to the nature and range of the cooling experiment, the effect of parameters such as source intensity, excitation frequency, Raman shift, mean value of the derived polarizability tensor, and temperature on the changes in dissolved methane band areas are assumed to be fairly minimal.

Figure 4 shows a series of Raman spectra (marked a though e) obtained from the bulk aqueous phase during an independent continuous cooling experiment on a quiescent methane-water system. Although separate, this experimental procedure was very similar to the visual continuous cooling experiment discussed earlier with regards to cooling rate, and initial cell pressure-temperature conditions (31.7 MPa and 24 ^{o}C). The final temperature in the Raman experiment was 2.8 ^{o}C. Spectra a and b correspond to 24 and 20 ^{o}C, respectively, when hydrates were absent. Spectra c, d, and e correspond to 15.6, 10.2, and 2.8 ^{o}C, respectively, when hydrates were present in the system. Hydrate film formation at the vapor-liquid interface was observed at 15.9 ^{o}C, and further cooling resulted in needle growth into the bulk aqueous phase, very similar to that shown in Fig. 2.

From Fig 4, in the absence of hydrates, the dissolved methane bands in spectra a and b were of comparable intensities. The intensity in spectrum b was slightly greater than that in spectrum a. This small increase in intensity with cooling agreed well with the expected increase in methane solubility upon cooling from 24 to 20 ^{o}C in the absence of hydrates (curve C_s (T) in Fig 3).

Upon cooling below 15.9 ^{o}C when hydrate nucleation followed by film formation was observed at the vapor-liquid interface, it can be seen from spectrum c in Fig 4 (at 15.6 ^{o}C) that there was a drop in intensity of the dissolved methane band. This implies that concentration of methane in the bulk aqueous phase decreased when the hydrate film formed at the vapor-liquid interface. This is in agreement with the decrease in equilibrium methane solubility predicted by Fig 3 due to the switch in solubility trends from C_s (T) before hydrate formation to C_{sh} (T) after hydrate formation.

Upon further cooling, spectra d and e in Fig 4 corresponding to 10.2 and 2.8 ^{o}C respectively, show that there was a significant decrease in the intensity of the dissolved methane band. The intensity in spectrum e was lower compared to that in spectrum d which in turn was lower than the intensity in spectrum c. This decrease in band intensity with cooling is indicative of a decrease in concentration of methane dissolved in water with decreasing temperature when hydrates are present in the system. This is in agreement with the opposite natures of the C_{sh} (T) curve and C_s (T) curves proposed in Fig. 3. Therefore, Raman spectra shown in Fig. 4 support the proposed mechanism that preferential hydrate needle growth occurred as a result of diffusion of methane from the bulk aqueous phase to hydrates at the vapor-liquid interface due to the decreasing solubility of methane in water with decreasing temperature.

3.4 Hydrate Dissolution During Stepwise Heating.

The second part of the visual experiment involved a stepwise heating of the cell from 5.2 ^{o}C, the temperature at the end of the continuous cooling process (Fig. 2f), to a final temperature of 23.4 ^{o}C. The intermediate temperatures were 10.5, 15.3, 20.3, 21.5, and 22.6 ^{o}C. The cell was held at each temperature for extended periods of time ranging from 20 to 80 minutes. Pressure and temperature profiles corresponding to the 5.5 hour stepwise heating process are depicted in Fig. 1. The expanded time scale was chosen to ensure sample equilibration at every stage. Fig. 1 shows that pressure increased during the heating process from 30.82 MPa at 5.2 ^{o}C to 31.6 MPa at 23.4 ^{o}C.

A sequence of images of the cell contents at different temperatures during the stepwise heating process is shown in Fig. 5 (a through f). It can be seen that an increase in cell temperature from 5.2 to 21.5 ^{o}C caused significant changes in the appearance and distribution of hydrate needles. Although not very clear from the image quality in Fig.5, it was observed that the sharp well-defined needles at 5.2 ^{o}C started to disintegrate and take on a diffuse less-defined appearance at 10.5 ^{o}C. An

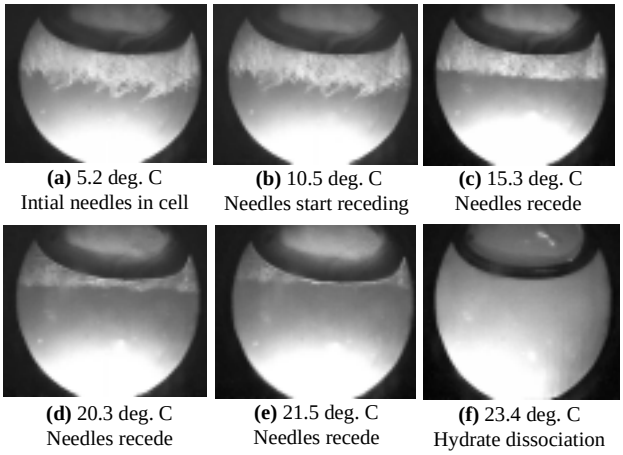

Fig. 5 A sequence of images of the cell contents at different stages of the stepwise heating process.

increase in the temperature to 15.3 ^{o}C caused further needle disintegration. The needle front, which had an irregular multi-faceted pointed appearance in Figures 5a and 5b, appeared to flatten out and recede toward the vapor-liquid interface. The 'hydrated' vapor-liquid interface however, continued to remain intact. Further increases in temperature to 20.3 and 21.5 ^{o}C caused further needle disintegration and needle front recession (Figs. 5d and 5e). At 21.5 ^{o}C, the needles had almost completely disappeared from the system. The 'hydrated' vapor-liquid interface was still intact.

Upon heating to 23.4 ^{o}C, which is 0.2 ^{o}C higher than the predicted hydrate dissociation temperature of 23.2 ^{o}C for a pressure of 31.6 MPa (using CSMHYD; Sloan, 1998), Fig. 5f shows that the hydrate phase was not stable anymore. Both the needles and the hydrate film at the vapor-liquid interface disappear.

Hydrate dissociation temperature is defined as the temperature at a given pressure when the final microscopic hydrate crystal disintegrates to yield liquid water and gas. However, from Fig. 5, it can be seen that hydrates were present in the cell throughout the stepwise heating process and do not disappear completely till the final temperature of 23.4 ^{o}C. This implies that hydrate dissociation per se corresponding to Lw-H-V equilibrium conditions occurred only at a temperature close to 23.4 ^{o}C. Needle disintegration, needle front recession, and shrinking of the hydrate phase upon heating was not hydrate dissociation. Instead, it was hydrate dissolution.

Hydrate dissolution can be explained using the solubility curves shown in Fig. 3 for methane in water in the absence and presence of hydrates. Equilibrium concentration of methane dissolved in water for five of the six temperatures in the stepwise heating process depicted in Fig. 5 (5.2 to 21.5 ^{o}C), would lie on the C_{sh} (T) curve corresponding to methane solubility in the presence of hydrates. It can be seen that the equilibrium solubility of methane in liquid water will progressively increase as the temperature of the system increased from 5.2 to 21.5 ^{o}C. Therefore, methane molecules had to be supplied to the bulk aqueous phase as the temperature increased from 5.2 to 21.5 ^{o}C.

The presence of a relatively impermeable hydrate film at the vapor-liquid interface effectively prevented the gas phase from supplying the methane molecules. Therefore, the hydrate phase (in the form of needles) was forced to supply the methane to the bulk aqueous phase. Since the surfaces and tips of the hydrate needles were in contact and hence in equilibrium with the aqueous phase, it is these surfaces and tips that dissolved in order to supply the methane molecules. This dissolution of needle surfaces and tips was responsible for the observed recession of the needle front in Fig. 5.

This phenomenon can be described in terms of phase equilibrium principles as a change in phase fractions of the hydrate and the aqueous phases with an increase in temperature. The driving force for such a change in phase fraction was the increase in equilibrium solubility of methane in water with an increase in temperature when hydrates are present in the system. As seen in Fig. 5, needle dissolution stopped when the water phase in contact with the needles attained the equilibrium methane solubility at a given temperature. Although not addressed in this paper, phase equilibrium principles also suggest that the molar composition of the hydrate phase formed from and in equilibrium with the bulk aqueous phase (in the effective absence of a free vapor phase) may be slightly different from composition of the hydrate phase formed in the presence of a free vapor phase, such as the hydrate film that first formed at the vapor-liquid interface during the cooling process.

The relatively flat appearance of the needle front in Figs. 5c and 5d compared to Figs. 5a and 5b is attributed to mass transport considerations. Since the needles that extend the most into the bulk aqueous phase are the ones in maximum contact with that phase, they will dissolve first upon heating to replenish the methane concentration of the bulk aqueous phase. As these needles recede and reach a point where their tips are lined up with all the other needles, then the preferential dissolution of those needles stops. Upon further heating, all needles along the front start to dissolve and recede simultaneously giving the front a flat uniform appearance.

At 21.5 ^{o}C (Fig. 5e), close to the predicted dissociation temperature T_{eq} of 23.2 ^{o}C, hydrates are principally present as a film at the vapor-liquid interface and as a layer on the window in the vapor phase. This is because, from Fig. 3, C_{sh} (T) and C_{s} (T) curves converge and intersect at T_{eq}. The close proximity of the solubility curves as temperatures approach T_{eq} will cause needles to almost completely disappear. An increase in temperature above T_{eq} should cause the hydrate phase to disappear altogether. This is evident from Fig. 5f. Therefore, the needle dissolution phenomenon during stepwise heating can be adequately explained using the solubility curves depicted in Fig .3.

4 Conclusions

Based on visual and Raman experiments, a mechanism is proposed for hydrate formation, growth, and dissolution in a quiescent methane-water system. It was observed that cooling the system caused hydrate film formation at the vapor-liquid interface followed by growth of hydrate needles into the bulk aqueous phase. Subsequent heating of the system caused progressive dissolution of needles until the three-phase liquid water-hydrate-vapor boundary was reached at which point hydrates became unstable altogether.

These phenomena are attributed to trends in methane solubility with temperature. The solubility of methane in water decreases with decreasing temperature in the presence of hydrates and increases with decreasing temperature in the absence of hydrates. These solubility

trends suggest that the aqueous phase became supersaturated with methane when hydrates first formed in the system during cooling. As a result, a concentration gradient was established resulting in diffusion of methane from the bulk aqueous phase to hydrate film at the vapor-liquid interface. Hydrate growth preferentially occurred in the form of needles due to heat transfer limitations arising from the quiescent nature of the system. The same solubility trends suggest that the opposite will be observed upon subsequent heating. An increase in temperature of the cell containing hydrate needles caused the aqueous phase to become undersaturated in methane which in turn set up a reverse concentration gradient that resulted in dissolution of needles to replenish the methane amount in the aqueous phase.

These results, although obtained for a quiescent system, have relevance for all types of hydrate formation processes. The driving force for hydrate nucleation is dependent on the extent of supersaturation and hence, on the solubility of the guest in the water phase. Therefore, solubility of guest molecules in the water phase is an important parameter that needs to be factored into models for kinetics of hydrate formation and growth.

References

Chalmers, B. (1964). *Principles of Solidification*, 2nd printing, John Wiley and Sons Inc., New York, USA.

Culberson, O.L., & McKetta, J.J. (1951). Phase equilibria in hydrocarbon-water systems, III-The solubility of methane in water at pressures to 10,000 psia. *Petroleum Transactions* **192**, 223-226.

Englezos, P., Kalogerakis, N., Dholabai, P.D., & Bishnoi, P. R. (1987). Kinetics of formation of methane and ethane gas hydrates. *Chemical Engineering Science* **42**, 2647-2658.

Englezos, P., Kalogerakis, N., Dholabai, P.D., & Bishnoi, P. R. (1987). Kinetics of gas hydrate formation from mixtures of methane and ethane. *Chemical Engineering Science* **42**, 2659-2666.

Freer, E. M. (2000). Methane hydrate growth kinetics. M. Sc. Thesis T 5400, Colorado School of Mines, Golden, USA.

Kimuro, H., Kusayanagi, T., & Morishita, M. (1994). *IEEE Trans. on Energy Convers*. **9**, 732.

Long, D. A. (1977). *Raman Spectroscopy*, McGraw-Hill, New York, USA.

Makogon, Y. F. (1996). *Proceedings of the Offshore Technology Conference*, Houston, Texas, May 6-9, pp. 749-756.

Ohmura, R., Shigetomi, T., & Mori, Y. H. (1999). Formaton, growth, and dissociationof clathrate hydrate crystals in liquid water in contact with a hydrophobic hydrate-forming liquid. *Journal of Crystal Growth* **196**, 164-173.

Skovborg, P., & Rasmussen, P. (1994). A mass transport limited model for the growth opf methane and ethane gas hydrates. *Chemical Engineering Science* **49**, 1131-1143.

Sloan, E.D. (1998). *Clathrate Hydrates of Natural Gases*, 2nd ed., Marcel Dekker, Inc., New York, USA.

Subramanian, S., & Sloan, E. D., Jr. (1999). Molecular measurements of methane hydrate formation. *Fluid Phase Equilibria* **158-160**, 813-820.

Subramanian, S., Kini, R.A., Dec, S.F., & Sloan, E.D., Jr. (2000). Evidence of structure II hydrate formation from methane + ethane mixtures. *Chemical Engineering Science* **55**, 1981-1999.

Sum, A. K., Burruss, R. C., & Sloan, E. D. Jr. (1997). Measurement of clathrate hydrates via Raman spectroscopy. *Journal of Physical Chemistry B* **101**, 7371-7377.

Szymanski, H. A., (1967). *Raman Spectroscopy – Theory and Practice*, Plenum Press, New York, USA.

Tulk, C. A., Ripmeester, J. A., & Klug, D. D. (2000). The application of Raman spectroscopy to the study of gas hydrates. *Annals of the New York Academy of Sciences* **912**, 859–872.

Uchida, T., Okabe, R., Mae, S., Ebinuma, T., & Narita, H. (2000). In situ observations of methane hydrate formation mechanisms by Raman spectroscopy. *Annals of the New York Academy of Sciences* **912**, 593–601.

Yamane, K., & Aya, I. (1995). Solubility of carbon dioxide in hydrate region at 30 MPa. *Proceedings of the International Conference On Technologies for Marine Environmental Preservation, Tokyo, Sep 24-29* **2**, 911.

Zatsepina, O., & Buffett, B. A. (1997). Phase equilibrium of gas hydrate: Implications for the formationof hydrate in the deep sea floor. *Geophysical Research Letters* **24**, 1567-1570.